PAPER

CrossMark
click for updates

Pneumatic stimulation of *C. elegans* mechanoreceptor neurons in a microfluidic trap†

Adam L. Nekimken,‡[ab] Holger Fehlauer,‡[b] Anna A. Kim,[bc]
Sandra N. Manosalvas-Kjono,[d] Purim Ladpli,[e] Farah Memon,[f] Divya Gopisetty,[b]
Veronica Sanchez,[a] Miriam B. Goodman,*[ab] Beth L. Pruitt*[abf] and Michael Krieg§*[b]

New tools for applying force to animals, tissues, and cells are critically needed in order to advance the field of mechanobiology, as few existing tools enable simultaneous imaging of tissue and cell deformation as well as cellular activity in live animals. Here, we introduce a novel microfluidic device that enables high-resolution optical imaging of cellular deformations and activity while applying precise mechanical stimuli to the surface of the worm's cuticle with a pneumatic pressure reservoir. To evaluate device performance, we compared analytical and numerical simulations conducted during the design process to empirical measurements made with fabricated devices. Leveraging the well-characterized touch receptor neurons (TRNs) with an optogenetic calcium indicator as a model mechanoreceptor neuron, we established that individual neurons can be stimulated and that the device can effectively deliver steps as well as more complex stimulus patterns. This microfluidic device is therefore a valuable platform for investigating the mechanobiology of living animals and their mechanosensitive neurons.

1 Introduction

Mechanical signals during touch and pain provide animals with crucial information about their environment, such as the proximity of a mate or potential predators. These forces are detected by receptor proteins within specialized cells that transduce mechanical stimuli into physiological signals, such as membrane depolarization or changes in gene expression. The transmission process that links mechanical stimulation of the cuticle to receptor activation has been difficult to investigate. Although techniques to activate mechanosensitive ion channels with forces in the piconewton range[1,2] have been applied to recombinant proteins and cultured cells *in vitro*, their

integration with whole-animal imaging of moving animals remains challenging, making it difficult to investigate mechanotransduction pathways in live animals. Similarly, although fluorescence imaging has provided researchers with tools to read out cellular physiology,[3] molecular dynamics,[4] and mechanical stresses[5–8] based on changes in a probe's fluorescence intensity, color, or lifetime, such imaging can be difficult to integrate with precise force application to moving animals.

The roundworm *Caenorhabditis elegans* is an excellent system to study mechanical stress transmission during touch, since its mechanoreceptors are well characterized on the molecular,[9,10] physiological,[11–13] and mechanical[5,14] levels. Genetic, molecular, and physiological tools to visualize forces on single molecules in live animals[14,15] are readily accessible. The transparent body of *C. elegans* facilitates high-resolution imaging down to the level of individual protein complexes.[5] The anatomy and molecular composition of *C. elegans* cuticle and its underlying epidermis (referred to as 'skin' hereafter) is very well characterized,[16] enabling manipulation and investigation of the skin's mechanics and its role in mechanosensation.[14]

C. elegans senses gentle mechanical loads delivered to its skin with six touch receptor neurons (TRNs) that tile the body of the worm in anterior and posterior tactile receptive fields (TRF).[10] According to their position in the animal's body, the anterior lateral TRNs are denoted ALML, ALMR, and the anterior ventral TRN is termed AVM. Analogously, the posterior

[a] *Department of Mechanical Engineering, Stanford University, Stanford, California, USA. E-mail: mbgoodman@stanford.edu, pruitt@stanford.edu*
[b] *Department of Molecular and Cellular Physiology, Stanford University, Stanford, California, USA. E-mail: michael.krieg@icfo.eu*
[c] *Department of Chemistry and Chemical Engineering, Chalmers University of Technology, Gothenburg, Sweden*
[d] *Department of Electrical Engineering, Stanford University, Stanford, California, USA*
[e] *Department of Aeronautics and Astronautics, Stanford University, Stanford, California, USA*
[f] *Department of Bioengineering, Stanford University, Stanford, California, USA*
† Electronic supplementary information (ESI) available. See DOI: 10.1039/c6lc01165a
‡ Shared first author.
§ New address: Institute of Photonic Sciences, ICFO, Castelldefels, Barcelona, Spain.

lateral TRNs are denoted PLML, PLMR, and the ventral is called PVM. From the cell body (soma) of each neuron, one single sensory neurite emanates anteriorly.[17] The mechanosensitive ion channels that are responsible for converting a mechanical stimulus into an electrical signal localize in the neurite.

The mechanosensitive channel is a sodium ion channel of the DEG/ENaC family and converts skin indentation into neuronal depolarization,[9] which leads to a change in the worm's behavior.[17] Loss of MEC-4, the key pore-forming subunit of the mechanoelectrical transduction channel responsible for detection of gentle touch in *C. elegans*, eliminates mechanoreceptor currents in TRNs[12] and causes insensitivity to touch stimuli.[18] In addition to electrical recordings, TRN physiology has been investigated using genetically encoded calcium indicators *in vitro*[19] and *in vivo*,[11,20–22] mainly by gluing live animals to agar pads using cyanoacrylate glue.[11,12,20,22] Although this strategy is compatible with mechanical stimulation *via* calibrated glass needles or other probes,[12,13] animals cannot be recovered for subsequent long-term studies. Additionally, the glue scatters light, complicating high-resolution imaging.

Microfluidic devices offer another strategy for immobilizing worms, either in a tapered channel,[23–25] by compressive immobilization,[26,27] or within an agar bed.[28] Various microfluidic devices have been reported that trap multiple animals for high-throughput imaging,[29] automated sorting,[30] quantification of muscular forces,[31] chemosensory analyses,[25,32] electrotaxis,[33,34] thermosensory analyses,[35,36] and whole-animal stress responses.[24,37] A long term culture platform for *C. elegans* based on microfluidic approaches has also been presented.[24,27] Here, we introduce a device that facilitates streamlined and high-resolution imaging of the mechanosensory response in combination with mechanical stimulation in *C. elegans*. Importantly, physical access to the immobilized worm is necessary for applying mechanical stimuli.

Our microfluidic device restricts the motility of a single worm for high-resolution imaging while delivering precise mechanical stimuli to the skin of the worm. We implemented a pneumatic actuation system in which a piezoelectric pressure pump drives a thin, deformable polydimethylsiloxane (PDMS) membrane that separates the pressure reservoir from the trapping chamber. Our device design is backed by analytical and numerical simulations predicting diaphragm deflections to optimize mechanical stimulation. The actuators are positioned along the immobilization chamber to target the activation of individual TRNs. The device is readily manufactured using standard soft-lithography techniques[38] (Fig. S1†) and can be integrated with widefield or confocal microscopy for fluorescence and transmission imaging. We demonstrated the performance of this device through high-resolution calcium imaging as a readout of TRN activity while applying mechanical stimuli and validated the performance predictions of our theoretical models. We propose that this device can be used to investigate current and future quantitative hypotheses about mechanoreceptor activation and mechanics.[10,14]

2 Results and discussion

2.1 Device overview

Our device consists of two integrated modules: an immobilization channel and six pneumatic stimulation channels (Fig. 1A). The inlet of the immobilization channel contains several pillars that facilitate loading of the animals in the desired orientation (head or tail first). Several animals can be 'parked' close to the inlet of the device. When a worm's head is near the trapping channel, we move it into the channel by applying pressure with a syringe, perform the experiment, remove the worm from the channel, and move on to the next animal. The outlet of the channel is slightly tapered
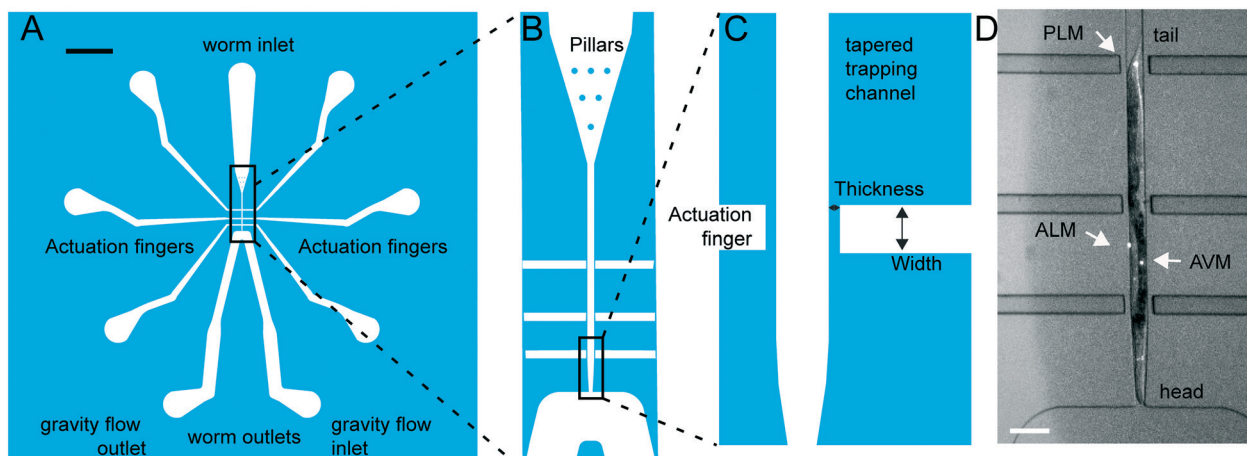

Fig. 1 Channel design overview. A: Overall device design with inlet, outlet, and air reservoirs. Scale bar = 1 mm. B: Enlarged view of the pillars for worm orientation, the tapered trap, and the air channels. C: Enlarged view of two of the six independent pneumatic actuators with their diaphragms and the tip of the tapered trap, which is 24 μm in width at its smallest point. D: Representative micrograph of a trapped worm; arrowheads point to the location of the TRN cell bodies. The mechanosensitive neurites extend anteriorly from the cell bodies toward the animal's head. Scale bar = 100 μm.

to fit the worm's tapered body shape and can be connected to a gravity flow reservoir that creates suction to keep the animal snug. The tapered end of the worm channel is 24 μm wide and restricts the animal from further forward movement. The shape of the channel snugly fits the worm's body and holds the animal in place for imaging. This geometry was adapted from a previous trapping device for exposing *C. elegans* to chemical stimuli.[32] In this position, the animal is located adjacent to three actuators on each side of the trap (six total). These actuators are thin PDMS membranes that deflect into the animal's body when pressurized from behind. They are positioned such that they are within the putative TRF along the process of each neuron. The actuators near the outlet are ≈250 μm from the middle actuators, which are ≈350 μm from the actuators near the inlet. We aligned the actuators along the trapping channel in order to stimulate the AVM and ALM TRNs on the worm's anterior side and the PLM and PVM TRNs on the worm's posterior side. The width of the actuators was chosen to match sizes of previously used indenters and to provide reproducible indentation performance. Each of the six actuators can be connected to individually controlled pressure reservoirs. After stimulation, the worm is removed from the trap through the outlet and is either discarded or collected for subsequent study. The latter feature could be used for longitudinal studies or to facilitate the characterization of many animals using calcium imaging of mechanosensitive neurons as a readout. Whereas worms can in principle also be removed through the inlet, removing them through the outlet one at a time significantly increases data acquisition and experimental throughput such that we were able to record from >20 worms in 3 h (data not shown).

2.2 Device design and simulations

To minimize the number of design iterations required for a functional and reproducible device, we performed analytical and numerical simulations to model actuator deflection under constant pressure. We estimated the deflection due to pressure of various actuator widths and diaphragm thicknesses with both analytical equations and finite-element simulations. We compared these *in silico* results with empirical measurements. We chose maximum deflection as the main metric for actuator design, because indentation is more strongly correlated with activation of the worm's touch receptor neurons than force.[20,39]

2.3 Analytical predictions of actuator performance

We designed the actuators to achieve a deflection of at least 7 μm (approximately one-third of the average radius of the worm). This is similar to the magnitude of indentations used in other studies.[11,13] First, we used an analytical model of a thin rectangular plate under uniform pressure to predict the resulting maximum deflection and the associated stress level. For a rectangular plate under uniform pressure, the maximum deflection is:[40]

$$w_{\max} = c_1 \frac{P \cdot L_{\min}{}^4}{E t^3} \tag{1}$$

where c_1 is a factor accounting for the aspect ratio and edge conditions of the plate, P is the uniform pressure applied to the plate, $L_{\min}$ is the smaller dimension of the edges of the rectangular plate, E is the Young's modulus of the material, and t is the thickness of the rectangular plate. Many values of c_1 are tabulated by Young and Budynas[40] for various edge conditions, but none of the tabulated values match the edge conditions of our device. Lee *et al.* found empirically that $c_1 = 0.0034$ accounts for the edge conditions of actuators with similar geometry,[41] consistent with our experiments.

We predicted the performance of various designs using a diaphragm height equal to the height of the trap channel, which is 50 μm, thickness of 10 μm, and a width of 50 μm (Fig. 2A).

2.4 Numerical prediction of actuator performance

Our analytical prediction was based on elastic plate theory and relied on assumptions that could reduce the accuracy of the prediction. The above equations assume that the Poisson's ratio of the material is 0.3,[40] the thickness of the diaphragm is small, and deformations are small and in the linear range. Because the deformations of the diaphragms in our device are likely to violate the assumption of small linear deformations and PDMS has a Poisson's ratio of 0.5,[42] we performed numerical simulations based on finite element methods. Our numerical simulations accounted for the boundary conditions, geometric nonlinearities, and material properties of the actual device. The plate theory described above requires assumptions about the boundary conditions of the thin plate. However, three sides of the diaphragm are connected to bulk PDMS, which is not a well-defined boundary condition. Because these three sides will behave differently than the bottom side, which is rigidly connected to a glass substrate, the behavior of the diaphragm at these junctions must be modeled in more detail to understand deviations from the analytical model.

Although PDMS can be assumed to be linear elastic up to 50% strain,[41] geometric nonlinearity still plays an important role in determining the maximum deflection and stress. The maximum deflection of the diaphragms we tested is in the range of 5–10 μm, which is on the same order of magnitude as the diaphragm thicknesses we tested (6–12 μm). The large deformation compared to the original state can cause the loading and boundary conditions to deviate from the idealized case. Further, since PDMS is relatively compliant, the hydrostatic pressure applied in the actuation channel causes the side walls to also deform during diaphragm deflection, reducing the amplitude of diaphragm deflection.

Fig. 2B shows the von Mises stress contour of an example simulation case (50 × 50 μm, 10 μm-thick diaphragm under 100 kPa of pressure). Note that the maximum stress of 0.5 MPa is predicted to occur at the center of the diaphragm
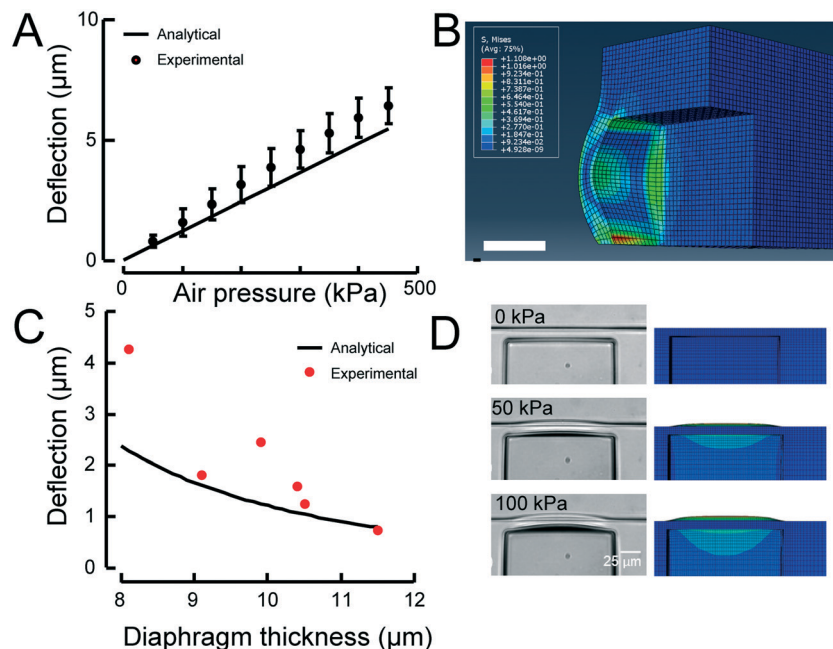
Fig. 2 Comparison of experimental measurements of diaphragm deflection to analytical and finite-element predictions. A: In the pressure range of interest, diaphragm deflection increases nearly linearly with applied pressure, in close agreement with the analytical simulations. Data are derived from measurements with a 10 μm-thick diaphragm and a 50 μm-wide actuator (black line). The variation in deflection could be attributed to variation in diaphragm thickness or material properties in the manufacturing process. B: Stress contour showing stress alleviation and stress concentration at PDMS–PDMS and PDMS–glass junctions respectively. Scale bar 20 μm. C: Experimental measurements of diaphragm deflection *versus* thickness for 100 kPa of applied pressure. Black solid line shows the analytical prediction. D: The shape of the deflected actuator in an experiment (left) matches the shape predicted by the finite element simulation (right).

edge that is bonded to the glass substrate (Fig. 2B). The magnitude of the maximum stress predicted by the finite element model (Fig. 2B) was comparable to that predicted using the analytical model (not shown). The stress on the sides connected to the bulk PDMS is lower than the side bonded to glass. This stress alleviation arises from the compliance of the PDMS, as the bulk PDMS is more compliant than rigid glass, causing the material to be more relaxed. The deformation of the bulk PDMS near the diaphragm edges decays to zero at points far from the diaphragm edges (Fig. 2D). The tensile strength of PDMS depends on the curing temperature.[41] Lee *et al.* reported that curing at 25 °C leads to an ultimate tensile strength of 5.13 ± 0.55 MPa and that curing at 100 °C leads to an ultimate tensile strength of 6.25 ± 0.84 MPa.[41,42] As a result, the PDMS (cured at 70 °C) in our device is not likely to fracture, and we never observed membranes that failed.

2.5 Experimental confirmation of actuator performance

To confirm the validity of our predictions, we fabricated six actuator designs that differed in channel width and diaphragm thickness. Deflections of 50 μm-wide, 50 μm-tall diaphragms were in good agreement with our elastic plate theory-based analysis (Fig. 2A). The experimental deflection measurements increased approximately linearly with increasing actuation pressure, which was reproducible over six experimental tests on a 10 μm-thick diaphragm. The maximum

standard deviation in the experiment was <1 μm (Fig. 2A), demonstrating that sub-micron displacement resolution was achieved with these devices. Our experimental deflection data matched the prediction of the analytical equation (solid line in Fig. 2C) for 100 kPa pressurization of diaphragms with different thicknesses.

The finite-element model also captured the shapes of the deflected diaphragm (Fig. 2D). The connection of the diaphragm to the bulk of the device increased the deformation at the edges of the diaphragm, as shown in Fig. 2D. The ratio of the diaphragm's thickness to its width and height is 1 : 5, causing it to behave more like a solid structure than a thin membrane. The finite-element model captured the deformation of the vertical side walls of the actuation channels, which are also compliant (Fig. 2D). This parasitic deformation of the vertical side walls negatively affected the deflection of the diaphragm by making the deflection less localized and reducing its amplitude, leading to the lower value of c_1 in eqn (1).[41]

To characterize the dynamics of the PDMS diaphragm, we used a piezo-driven pressure pump capable of delivering 450 kPa to apply several pressure profiles. First, We applied a step (Fig. S2A†) and a ramp (Fig. S2B†) to measure the rise time of the diaphragm deflection. We report the 10–90% rise time ($t_{10–90}$) or the time needed for the pressure and diaphragm position to change from 10 to 90% of the final value. The time lag between the pressure ($t_{P,10–90}$) and the deflection ($t_{D,10–90}$) determined in this way from three independent

diaphragms was $(t_{D,10-90} - t_{P,10-90}) = 20 \pm 3$ ms (mean ± SD; N = 3) and we noticed a slightly non-linear response (Fig. S2A†). We repeated the same analysis for the fall time and found an average time lag between pressure and deflection of 30 ± 16 ms. The ramp with a pressure increase of 137.5 kPa s^{-1} lead to a deflection increase of 2.4 ± 0.5 μm s^{-1} (mean ± SD; N = 3). We repeated the analysis for a 10 Hz sinusoidal pulse of 150 kPa (peak-to-peak) superimposed on a 275 kPa step and monitored the deflection of the diaphragm (Fig. S2C†). The deflection (D) followed the pressure (p) with minimal attenuation of the maximal deflection compared to the steady state deflection for the same pressure (13%, sd = 6%, N = 4). By fitting sinusoidal functions to the 10 Hz sinusoidal pressure pulse and the resulting deflection we estimated the phase shift in all three traces to be below 0.08 rad (corresponding to ≈1 ms) which is well below the resolution limit of our imaging procedure. Note that the natural frequency of the diaphragm is more than 100 kHz,[43] so the mechanics of the diaphragm itself do not affect the speed of actuation. The maximum strain rates at these pressure differentials are ≈120 μm s^{-1} for the step stimulus and ≈50 μm s^{-1} for the buzz stimulus. The output frequency matches the input frequency and no dispersion or signal deterioration is visible in the power spectrum.

Taken together, our experimental measurements corroborated our analytical and finite-element simulations. Based on these data, for our final devices, we chose 10 μm-thick, 50 μm-wide diaphragms. Our simulations and experimental results indicated that 450 kPa of actuation pressure result in 6.4 μm of deflection with this design. We chose 50 μm as the width of the actuators so that the stimulus would be more localized and therefore more comparable to previous studies that used glass rods[12] or beads[39] to stimulate the worm. We chose 10 μm as the thickness of the diaphragms because it was easier to fabricate these devices than the 8 μm-thick devices.

2.6 Alternative design considerations

We designed the width of the actuator to match the order of magnitude of indenters that have been used previously by us and other groups to apply localized touch stimuli.[39] However, there is a trade-off between the minimum width of the actuator and the indentation depth. The maximum deflection scales with the fourth power of the smaller side length of the actuator (eqn (1)), while increases in pressure are limited by the supply and the connections. As a result, alternative connectors could increase the maximum amount of delivered pressure.[55]

Additional actuators beyond the six in our device can be implemented to improve the device's ability to stimulate the animal at various locations. For example, a 300 μm neurite could be stimulated by three 50 μm-wide actuators with 75 μm between the actuators. If the actuators are too close, however, a parasitic deformation of neighboring channels can interfere with precise stimulus application (Fig. 2B). We did not design the device specifically to study the spatial distribution of the worm's TRF, so we chose to put only enough actuators to stimulate any of the worms TRNs.

2.7 Performance of the trapping design

To hold the animal in place during mechanical stimulation, we modified a previously reported trapping system[25] consisting of a square channel 50 × 50 μm, which fits an adult worm (see Methods for detailed dimensions of the trap). The nozzle is 24 μm wide and tapers to expose the worm's nose to a flow channel, such that the nose could be exposed to biologically active substances and buffer solutions (Fig. 1C). An animal is loaded into the channel and precisely positioned by applying a pressure difference across the inlet and outlet, driving liquid through the device. The inlet contains several pillars (Fig. 1B) that cause the worm to crawl around the loading chamber. When the worm's head points toward the trap, pressure is again applied to the inlet to carry the worm into the trapping chamber, where it fits snugly within the channel with its head exposed to the outlet. The reverse orientation could be achieved, if the pressure is applied when the tail points forward. The outlets are connected to a gravity flow reservoir, which stabilizes the worm within the trapping channel (Fig. 1A and D). To remove an animal, we increase the pressure at the inlet with a manual syringe, forcing the worm through the channel and out of the device.

To test the viability of released animals at the end of this procedure, we released several animals through the narrow nozzle and let them lay eggs for 16 h on a fresh agar plate and then counted the number of progeny. Importantly, all worms survived the trapping and release procedure and laid eggs, although stimulated worms laid fewer eggs than untreated animals (38 ± 14 vs. 73 ± 12; mean ± SD; N = 10 animals).

2.8 Indenting the worm

To analyze the indentation of the worm under constant pressure, we stained an animal with the lipophilic dye DiI (1,1′-dioctadecyl-3,3,3′,3′-tetramethylindocarbocyanine perchlorate; as in Schultz et al.[44]) to visualize its skin, then inserted it into our device. Microscopy verified that the worm's forward and backward motility inside the channel was minimal. In this position the tail of the animal is still wiggling, allowing us to confirm that trapped animals were alive. We also observed a deflection of the diaphragm away from the trapping channel, presumably due to the pressure of the worm inside the channel (Fig. 3A). Thus, initial strain in the worm's tissues may lead to nonlinearities in the mechanical behavior when indenting the worm.[45]

We imaged the animal before and during the application of external pressure using a confocal microscope, acquiring a complete z-stack before (Fig. 3A) and after (Fig. 3B) stimulation. Using a calibrated pixel count, we estimated the maximum deflection of the diaphragm into the worm to be 7 μm relative to the membrane position with no applied pressure.
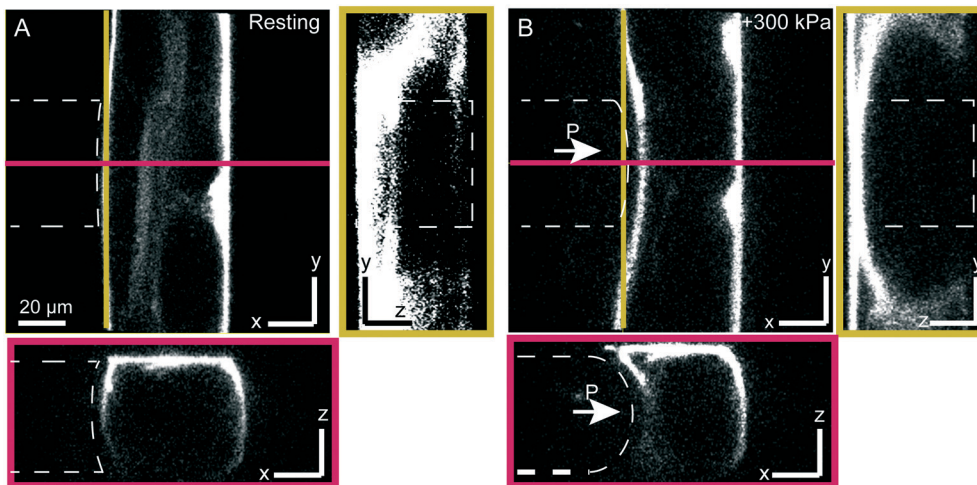
Fig. 3 Mechanical deformation of a live *C. elegans* in the microfluidic chip. Confocal slices through trapped animal stained with DiI in a 50 × 50 μm channel diaphragm before (A) and during (B) application of *p* = 300 kPa to the pressure channel (outlined with a white dashed line). Left panels depict the *yz*-plane along the yellow line; the bottom panels show the *xz*-plane along the red line.

Together, these results establish that the device suitably restricts animal motility for delivery of precise micrometer-sized mechanical indentations (Fig. 2A) that deform the animal's body (Fig. 3B). Because all animals survived this procedure, we envision that these devices can be used for genetic screens targeted to investigate mechanoreceptor activation and to perform longitudinal studies.

2.9 TRNs are activated by blue light

Next, we used our device to trap transgenic animals expressing the genetically encoded calcium indicator GCaMP6s exclusively in TRNs (TRN::GCaMP6s). Our goal was to use this indicator to detect TRN activation after mechanical stimulation in the chip. In our initial experiments, exciting TRN::GCaMP6s with blue light was sufficient to elicit a large increase in the fluorescence of the lateral TRNs (ALM and PLM) in the absence of a mechanical stimulus (Fig. 4A). Although mechanically-induced calcium transients were superimposed on the light-induced response (Fig. S3†), it was challenging to differentiate between mechanically- and optically-induced signals. We therefore sought to genetically disable the light-induced signal. *C. elegans* expresses LITE-1, a known receptor for blue light in neurons ASH and ASJ, as well as other head neurons,[46,47] and blue light evokes avoidance responses reminiscent of those activated by touch.[48]

We mined a single-neuron RNA-seq database (Accession # SRR3481678, SRR3481670, SRR3481680 and Lockhead *et al.*[49]) to compare the expression pattern of *lite-1* in various neurons and found that *lite-1* is expressed at high levels in the PLM TRN, but not in the chemosensory neuron ASER or the thermosensory neuron AFD (Fig. 4B). As expected if *lite-1* functions as a blue-light receptor in TRNs, *lite-1(ce314)*;TRN::GCaMP6s mutants lacked light-induced TRN::GCaMP6s signals in the lateral TRNs (Fig. 4A) and avoidance responses (Fig. 4C). This genetic background sup-

presses light-evoked calcium transients in the TRNs. These experiments establish that *lite-1* is necessary to induce light-sensitive calcium transients in lateral TRNs.

We determined that *lite-1(ce314)* mutants retain wild-type touch sensitivity by conducting a well-established behavioral touch assay[50] in which we touched an animal's body 10 times with an eyebrow hair. A change in behavior (such as the animal accelerating, pausing, or reversing its movement directionality) was scored as a positive response. In agreement with previous results,[5] wild-type animals (N2) showed an average response frequency of 90.5 ± 1% (mean ± SD; *N* = 100 animals), whereas the average response frequency decreased to 23 ±4.7% (means ± SD; *N* = 100 animals) in *mec-4(u253)* mutants, which lack the pore-forming subunit of the mechanosensitive ion channel (Fig. 4D). With *lite-1(ce314)*-mutant worms, this touch assay yielded results similar to those from wild-type worms (95 ± 5%; *N* = 75 animals), indicating that *lite-1* is necessary for light (Fig. 4A and C), but not for touch sensation (Fig. 4D). Further, the touch response in wild-type and in *lite-1(ce314)*-mutants was not altered by the expression of TRN::GCaMP6s, while *mec-4(u253)*;*lite-1(ce314)*;TRN::GCaMP6s mutants were indistinguishable from *mec-4(u253)* single mutants (Fig. 4D).

2.10 Mechanical activation of TRNs

Next, we investigated the cellular basis of the touch-induced behavioral response by performing calcium imaging of the mutant *lite-1(ce314)*;TRN::GCaMP6s, with the double mutant *lite-1(ce314)mec-4(u253)*;TRN::GCaMP6s as a negative control.

To establish whether our device differentiated among responses to multiple stimulus profiles, we designed a protocol consisting of a 275 kPa step (delivering ≈4 μm indentations), a 275 kPa ramp, and a 75 kPa, 10 Hz sine superimposed on a 275 kPa step (buzz stimulus, Fig. S2†). A similar indentation magnitude was previously shown to induce mechanoreceptor currents in live animals to each stimulus.[13] A 10 Hz stimulus
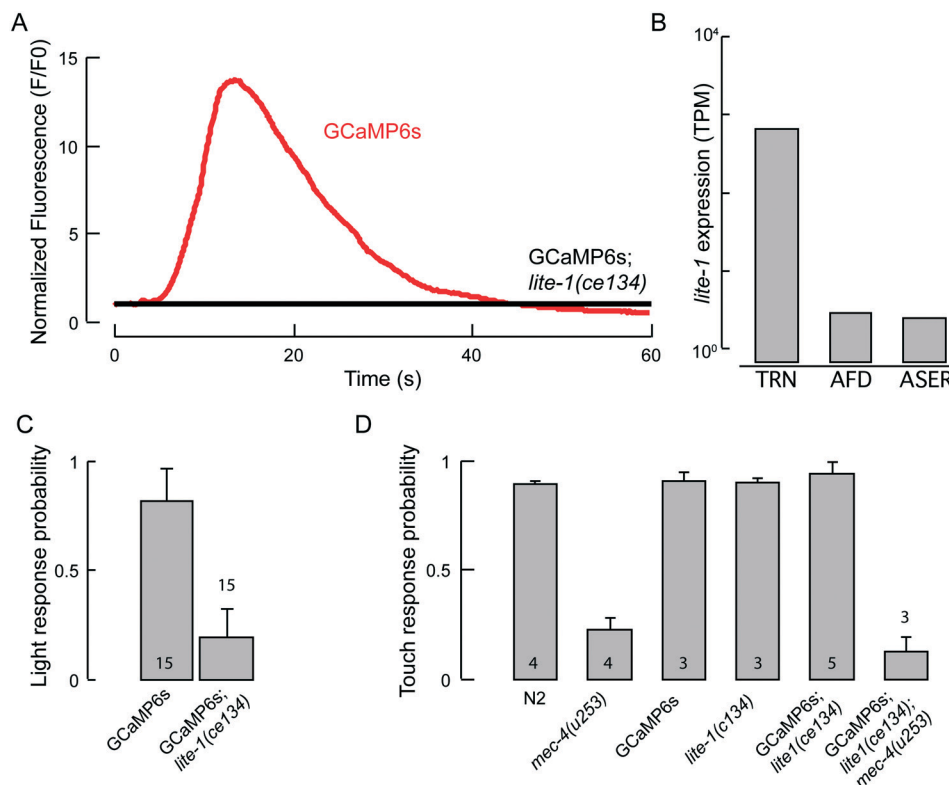
Fig. 4 Light- and force-sensitive behaviors of *C. elegans* strains. A: A representative trace of TRN::GCaMP6s fluorescence intensity in the ALM TRN after illuminating a single worm with blue light in TRN::GCaMP6s control (red) and TRN::GCaMP6s;*lite-1(ce314)* mutants (black). *N* = 10 worms have been imaged. Signals were normalized to the first 10 frames in after illumination. Note, difference in baseline might be due to calcium influx directly upon illumination with blue light. B: Quantification of *lite-1(ce314)* expression in PLM TRN by RNA-seq, in number of *lite-1* mRNA reads found per million reads.[49] C: Wild-type worms are more likely to show an avoidance response to blue light than *lite-1(ce314)* mutants when illuminated with 7 mW mm^{-2}. Means and standard deviations are shown (*N* = 15). D: Touch response of *lite-1* and TRN::GCaMP6s transgenic animals. Mutants (TRN::GCaMP6s;*lite-1(ce314)*) and *mec-4(u253)*, double mutants (TRN::GCaMP6s;*lite-1(ce314)mec-4(u253)*), and wild-type (N2) worms were assayed. Numbers in the bars indicate the number of independent experiments. In each experiment, 25 animals were touched 5 times with an eyebrow hair on the head and the tail in an alternating manner (10 touches in total per animal). Mean ± standard deviation.

was chosen because previous reports indicated a much stronger activation with dynamic motion of the probe as compared to a static stimulus.[11,13] The origin of this effect is currently under debate.[10,13]

We stimulated ALM, AVM and PVM using one of the six actuators which was located closest to their cell bodies within their presumptive TRFs (green overlays in Fig. 5 panel i). Though we observed calcium transients in PLM we did not include them into our analysis: the position of the PLM cell body is in the tip of the worms tail which could not be immobilized in the chip. This led to out-of-focus movement limiting the accuracy of the measurements of the PLMs calcium transients.

To our surprise, the application of the step or the ramp stimulus (Fig. 5A–C and Movie S1†) gave no detectable response from the TRNs at these pressure amplitudes when stimulated within their TRF. In agreement with previous reports,[11,13] we observed strong activation of each TRN after application of the buzz stimulus, which was visible as an increase in GCaMP6s fluorescence in the cell body and the neurite (Fig. 5D–F). The activation in response to the buzz stimulus consistently occurred with strong calcium transients

in anterior TRNs ALM and AVM (Fig. 5A and B) but also activated PVM neurons (Fig. 5C), despite the fact that they are dispensable for behavior.[51,52] Application of the maximum pressure of 450 kPa also induced calcium transients after a step and a ramp stimulus (Fig. S4;† *N* = 10 animals). Interestingly, the activation of PVM to the step stimulus at these high pressures was consistently higher than in the anterior neurons. However, the increase in fluorescence intensity in either neuron due to the step was never as large as that elicited by a buzz. In agreement with previous reports,[20] there was no correlation between the maximum GCaMP6s intensity observed in each neuron with the distance of the cell body to its nearest actuator (Pearson's rank correlation coefficient, 0.03, *P* = 0.81). Importantly and consistent with the existence of a tactile receptive field, this activation only occurred when the TRNs were stimulated in an area overlapping with their sensory dendrite, but not outside of it. When we stimulated ALM and imaged the activation of PVM, we never observed calcium transients in these neurons (Fig. 5, panel iv). Likewise, no calcium transients were observed when we stimulated PVM and imaged AVM/ALM. Taken together, these results are consistent with prior reports that found mechanoreceptor
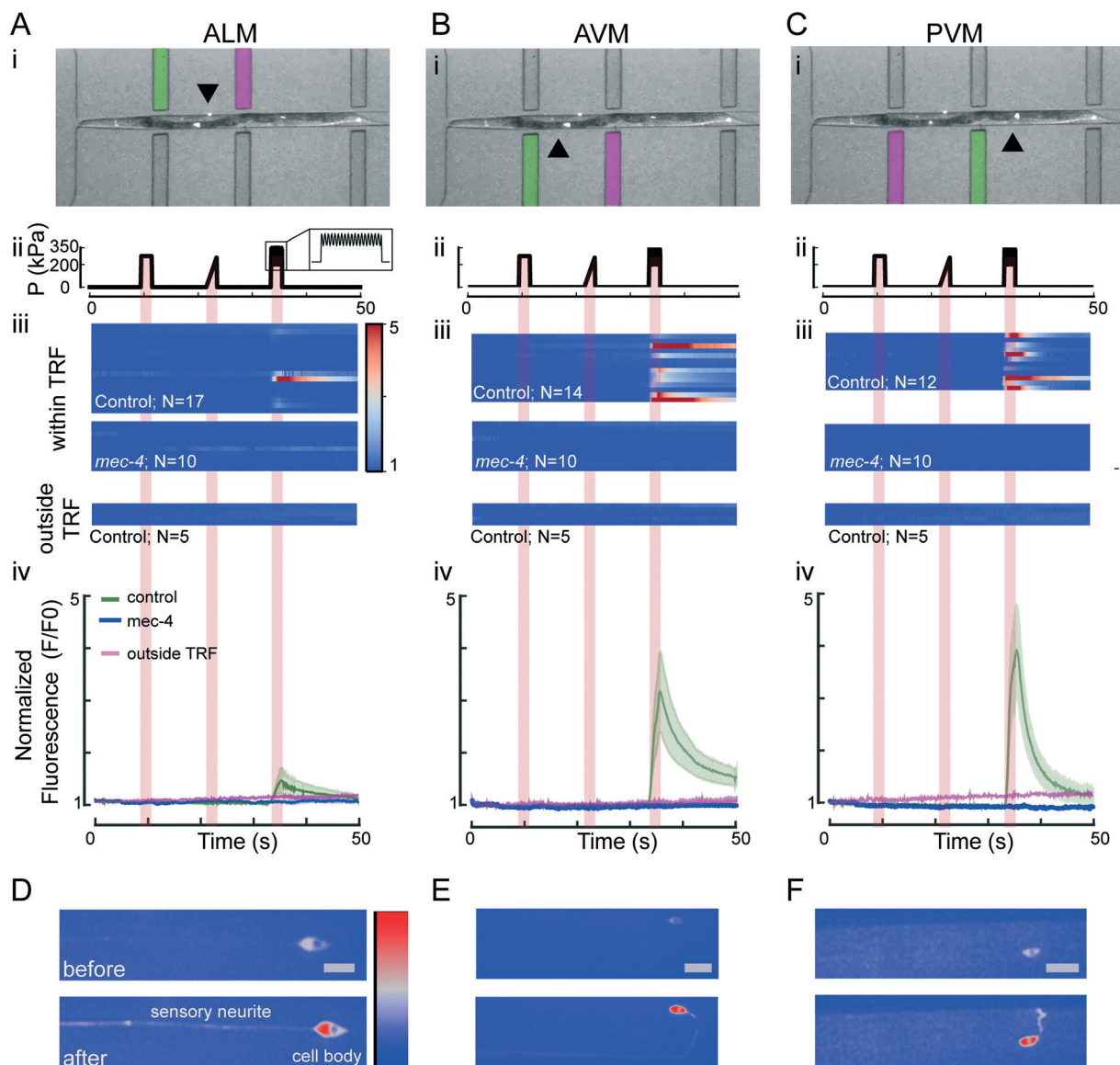
Fig. 5 Calcium dynamics of TRNs as a response to a step, ramp and buzz stimulus within and outside their presumptive tactile receptive fields (TRF). A–C: Response dynamics of ALM (A), AVM (B) and PVM (C) touch receptor neurons stimulated within and outside their TRF. (i) Overlay of a brightfield and a fluorescence image showing a worm in the microfluidic chip. The actuator used for stimulation of the respective neuron within its receptive field is marked in green, and the actuator used to stimulate each neuron outside its TRF is marked in magenta. The arrows point toward the cell body of the neuron of interest. (ii) Stimulus protocol including 2 second diaphragm excitation representing a 275 kPa step, a 275 kPa ramp and a sine (75 kPa; 10 Hz) superimposed with a 275 kPa step (buzz). (iii) Multiple false color-coded normalized fluorescence intensity traces (F/F_0) during the mechanical stimulation (shown in (ii)) of lite-1(ce314);TRN::GCaMP6s (control) and lite-1(ce314)mec-4(u253);TRN::GCaMP6s (mec-4) mutant animals and of control animals stimulated outside their TRF. (iv) Average fluorescence intensity (F/F_0) of the traces shown in (ii) for control (mean ± SEM as green shaded area, $N = 17$ for ALM, $N = 14$ for AVM, $N = 12$ for PVM) and mec-4 mutant animals (mean ± SEM in blue with $N = 10$ animals for ALM, AVM, and PVM) when stimulated within their TRF and the average fluorescence intensity of five traces of each TRN when stimulated outside their TRF (magenta). The positive slope could be attributed to differential bleaching in the red and green channels. D–F: Representative high-resolution images of ALM, AVM and PVM neuron before and after stimulation within their TRF. Color scale = 1500–3500 gray values and scale bar (=10 μm) for all images.

currents have a greater magnitude for sinusoidal stimuli[11,13] delivered to their tactile receptive field.

While all TRNs responded to a buzz stimulus (Fig. 5) delivered to the most proximal actuator, the ventral TRNs (AVM and PVM) displayed larger responses (Fig. 5) and higher response probabilities. We also found that the signal decayed more rapidly to baseline levels in PVM (with a time constant of 3.7 s ± 5.4 s, mean ± SD, $N = 9$) than in AVM (9.2 s ± 3.2 s, $N = 11$) and ALM (8.2 s ± 5.4 s, $N = 6$) (Fig. 5A–C panel iii). In all experiments conducted with wild-type animals, we found that 63% of ALM neurons, 92% of AVM and 81% of PVM neurons reacted to a stimulus given by the proximal actuator. A potential explanation for the different activation probabilities between lateral and ventral TRNs could be the smaller

deflection of the actuator (Fig. 2D and 3) near the cover glass where the processes of the lateral TRNs are usually found. The processes of the ventral TRNs are usually near the middle of the actuator, where the actuation amplitude is largest (Fig. 2D and 3). We thus sought to investigate how ventral neurons responded when stimulated on their opposite side, *e.g.* dorsal of the body axis (Fig. S6†) and used AVM to test this question. To our surprise, we did not detect an influence of the side the stimulus was given on the activation strength

and probability of AVM (Fig. S6†). This observation was also independent of which side the stimulus was given first. Taken together, we could not detect a limitation of the TRF of AVM along the dorsal-ventral body axis.

Importantly, indentation-evoked calcium signals depended on the presence of MEC-4, an essential, pore-forming subunit of the ion channel responsible for the sense of touch in *C. elegans*.[12] In *mec-4(u253)* mutants lacking a functional mechanosensitive ion channel, we never observed any changes in calcium-dependent GCaMP6s fluorescence in TRNs (Fig. 5). These data confirm that the stimuli supplied through our microfluidic device mimic the gentle touch stimuli that activate TRNs and are thus physiologically relevant in order to study the *C. elegans* touch response. We also used this device to investigate the presumptive tactile receptive field in anterior–posterior and dorso-ventral direction. Consistent with previous results from mechanical[11] stimulation of wild-type TRNs and optogenetic stimulation of channelrhodopsin-expressing TRNs,[53] we also observed a mild reduction in fluorescence intensity after sequential mechanical stimulation (Fig. 6), indicative of habituation to a repeated mechanical signal. This showcases the ability of this device to study changes in touch sensation in individual animals. Additionally, future studies will have to investigate how TRN activation differs in mutants that are not easily scored in classical behavioral assays.

3 Conclusion

We have designed and deployed a simple microfluidic device that integrates mechanical stimulation with high-resolution imaging of single worms. We performed analytical and finite-element simulations to inform our design. Our experimental measurements were in agreement with data from these simulations. Our device empowered investigations of the physiological and molecular basis of touch sensation. By detecting TRN activation with a calcium-sensitive fluorescence indicator, we confirmed that TRN activation is frequency-dependent *in vivo*. Thus, this device can be used to investigate the molecular nature of the proposed high-pass filter in *C. elegans* TRNs.[10,13] Taken together, our results establish that this microfluidic device exerts physiologically relevant stimuli and can be used to achieve quantitative deconstruction of the molecular and mechanical foundations of the touch response *in situ*.

4 Materials and methods

4.1 Finite-element simulation

We modeled device diaphragms in ANSYS Mechanical APDL with various design dimensions using tetrahedral elements. The vertical sides are merged with a body of bulk PDMS ($50 \times 50 \times 50$ μm, large enough such that local effects do not reach the edge of the model). The top side is connected (merged) to a layer of excess PDMS (30 μm). The edge connected to the glass substrate is modeled as a rigid boundary condition,
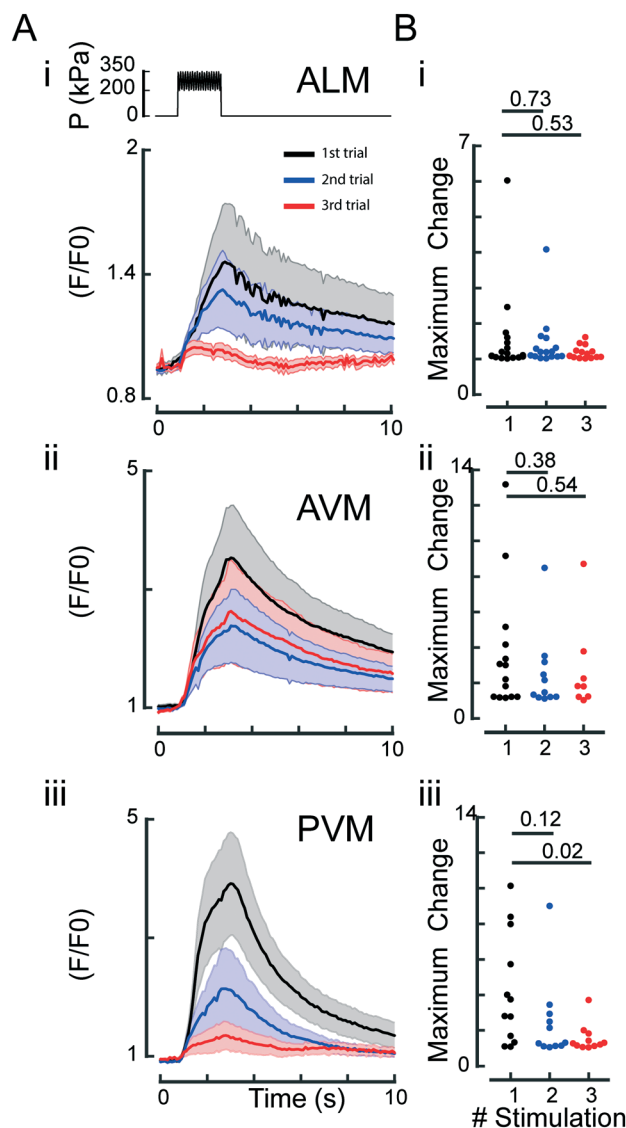

Fig. 6 Repeated mechanical stimulation of TRNs cause habituation of the calcium response. A: Response dynamics of ALM (i), AVM (ii) and PVM (iii) to three sequential buzz stimuli with an inter-stimulus interval of 1 min. Top panel in (i) shows the schematic representation of the stimulation protocol. A 75 kPa oscillation was superimposed to a 275 kPa step for 2 s. Normalized TRN::GCaMP6s fluorescence for three sequential stimuli. Black traces, fluorescence during the first stimulus; blue traces, fluorescence during the second stimulus; red traces, fluorescence during the third stimulus. Means and standard error of the mean ($N = 10$) are shown. B: Peak amplitude after sequential stimuli. Numbers above individual data points represent *P*-values according to Wilcoxon test for statistical significance.

since glass is much stiffer than PDMS. The rest of the external surfaces are also rigidly clamped since they are adequately far from the diaphragm.

During the simulation, a uniform pressure is applied on the inside surface of the diaphragm. We used a mesh size of 2.5 μm to capture large deformations. Any nonlinear geometry/deformation is allowed, and the simulation takes place in increments (with a minimum of 1×10^{-5} of the total time step) to ensure convergence. We assumed that PDMS behavior is isotropic and linearly elastic, with a Young's modulus of 1.75 MPa (10:1 mixing ratio, 70 °C curing temperature) and a Poisson's ratio of 0.5.[42]

4.2 Device layout

We designed transparency masks using L-edit (Tanner Research, Inc.) for prototyping device designs and process parameters. Our final devices were designed in AutoCAD (Autodesk, Inc.) and were fabricated from a chrome mask (Compugraphics) because we were unable to resolve small actuator diaphragms with a transparency mask.

In order to determine the optimal trap geometry, we fabricated two independent designs for young adult worms and L4 worms, each with three actuators on either side of the trap. Actuators are placed 250 μm (young adults) or 230 μm (L4 worms) from the narrowest part of the trap to the middle of the first actuator. The middle set of actuators are 500 μm (young adults) or 460 μm (L4s) from the narrowest part of the trap to the middle of the second actuator. Finally, the distance from the narrowest part of the trap to the middle of the third actuator is 850 μm (young adults) or 782 μm (L4s). The trapping channels are 50 × 50 μm in cross-section for young adults and 45 × 45 μm in cross-section for L4s. The tapered part of the channel nearest the nose of the animal is 24 × 50 μm or 24 × 45 μm.

4.3 Device fabrication

Device fabrication is a one-mask process that utilizes standard soft-lithography techniques. Briefly, we used SU-8 photoresist to create molds on wafers. To decrease the risk of delamination of the SU-8 features from the wafer, we exposed a 2 μm-thick SU-8 adhesion layer across the entire wafer with no mask and post-baked it prior to depositing and patterning the 50 μm SU-8 layer. We then silanized (chlorotrimethylsilane for 30 minutes) the molds and cast PDMS onto the mold. After curing the PDMS at 70 °C, we diced the devices and punched holes for fluidic connections using a biopsy punch. Finally, we plasma-activated the devices and bonded them to coverslips (#1, VWR).

4.4 Worm strains

The following strains were used for this study: N2 (Bristol); AQ3235 *ljSi1 (mec-7p::GCaMP6s+cb-unc-119(+))*; GN581 *ljSi1*; *mec-4(u253)*; GN692 *ljSi1;lite-1(ce314)*; GN693 *ljSi1;mec-4(u253)lite-1(ce314)*. AQ3235 was a kind gift from W. R. Schafer (Cambridge UK).

4.5 Nematode strains and culture

Animals were synchronized, grown at 20 °C, and used for experiments 48 h after synchronization, in accordance with standard protocols.[54] Wild-type (N2) worms were obtained from the *Caenorhabditis* Genetics Center, which is funded by National Institutes of Health Office of Research Infrastructure Programs (P40 OD010440). Transgenic strain AQ3235 *(ljSi1[Pmec-7::GCamp6s; cb-unc-119(+)])* was obtain from William R. Schafer and outcrossed twice to obtain with TU253 or KG1180 to get GN581 and GN692, respectively. We then crossed GN692 with TU253 to get GN693.

4.6 Worm loading and device performance

Individual animals were picked into a droplet of filtered M9 (Nalgene syringe filter, 0.22 μm, Thermo Scientific) and drawn into polyethylene tubing (0.9652 mm OD, 0.5842 mm ID, Solomon Scientific) connected to a 1 ml syringe (BD). The end of the tube was connected to the inlet of the microfluidic chip (Fig. 1A) using small metal tubing (0.635 mm OD, 0.4318 mm ID, 12.7 mm long, New England Small Tube Corporation). By gently depressing the plunger of the syringe, individual animals were transferred into the inlet of the device and pushed into the trapping channel until one worm ended up in front of the actuation channels.

Individual actuation channels of the microfluidic device were connected to an Elveflow pressure pump (OB1 controller equipped with 0–800 kPa pressure channel) with the same polyethylene and metal tubing as the worm inlet. The highest available pressure was 450 kPa, limited by the input pressure available to the pressure pump. The pressure outlet of the OB1 controller was connected to the microfluidic tubing using the following equipment: Water-Resistant Clear Polyurethane Tubing, 4 mm ID and 6 mm OD (McMaster-Carr, 5195 T52); Water-Resistant Clear Polyurethane Tubing, 2.6 mm ID and 4 mm OD (McMaster-Carr, 5195 T51) connected by Push-to-Connect Tube Fitting for Air, and a Straight Connector for 6 mm × 1/4″ Tube OD (McMaster-Carr, 5779 K258). A custom pressure protocol was preset within the Elveflow software and applied during the experiment. The protocol consists of a 10 s wait at 0 kPa, 2 s pressure step of 275 kPa, another 10 s wait at 0 kPa, a 2 s linear ramp to 275 kPa, another 10 s wait at 0 kPa, a 2 s with 75 kPa sine amplitude superimposed on 275 kPa step (buzz stimulus), and a final 10 s wait at 0 kPa.

Deflection of the diaphragm was measured using brightfield microscopy images (Leica DMI 4000 B microscopy system, 63×/1.32 NA oil objective (Leica) and a Hamamatsu Orca-Flash 4.0LT digital CMOS camera) taken at 100 frames per second using an ROI of 10 by 70 pixels during the pressure application. The edge of the diaphragm was tracked in each frame using custom ImageJ procedures.

4.7 Behavioral analysis

Assays of touch sensitivity were carried out as described.[50] In short, an eyebrow hair was glued to a wooden stick and

gently stroked over the anterior and posterior of the worm in an alternating manner for a total of ten trials per animal tested. For each experiment, 25 animals have been assayed over the course of N days (Fig. 4D). Responses were scored for each hair stroke and averaged per day to created Fig. 4.

For the blue-light assay, synchronized young adult animals expressing TRN::GCaMP6s were illuminated in brightfield under a fluorescence stereo microscope (Nikon SMZ18) using 2× magnification. The fluorescence shutter was opened to illuminate a single animal with 7 mW mm^{-2}, 488 nm blue light. A response was scored as positive if the animal changed its behavior within 2 s of exposure to blue light. The response in control animals (TRN::GCaMP6s) was accompanied by an increase in fluorescence intensity.

4.8 Confocal imaging

Live animals were stained with DiI as previously described[44] and mounted in the 50 × 50 μm trapping channel with an 8 μm diaphragm as described above. Imaging was performed on a Leica SP8 confocal system equipped with a 63×/1.4 oil immersion lens, a 1.5 mW white light laser tuned to 540 nm and a spectral detection system using a prism spectrometer-based emission separation tuned to capture a band between 550–650 nm. To visualize the deformation imposed by the actuator, we imaged z-stacks composed of 88 frames separated by 1 μm.

4.9 Calcium imaging

In vivo calcium imaging of TRNs was performed on a Leica DMI 4000 B microscopy system (Lumencor Spectra X light engine, fluorescence cube with beam splitter (Chroma, 59022bs), 63×/1.32 NA oil objective (Leica), Hamamatsu W-view Gemini Image splitting optics with beam splitter (Chroma, T570lpxr) and emission filters (Chroma, ET525/50m and ET632/60m), and a Hamamatsu Orca-Flash 4.0LT digital CMOS camera). Cyan (0.77 mW) and yellow (1.21 mW) illumination from the light engine was used to excite green TRN::GCaMP6s and red mCherry fluorescence in the TRNs. mCherry fluorescence was recorded to correct for defocusing artifacts during image analysis. The emission spectra were split by the image-splitting optics and projected onto separate parts of the camera chip. To follow calcium transients, image sequences were recorded at a rate of 10 frames-per-second. To control for potential habituation to repeated stimuli (Fig. 6) when testing the same neuron ventrally and dorsally with sequential stimulus protocols, we alternated the sequence of which side was stimulated first. To map the dorsoventral TRF, for example, we applied the first stimulus to the ventral side and the second to the dorsal side and alternated this sequence in a second data set (Fig. S6†). No randomization was performed in the step, ramp, buzz test.

4.10 Image analysis

All image sequences were analyzed with an in-house Fiji program (Fig. S5†) available for download on GitHub (https:// github.com/HFehlauer/Poking-Analyzer/blob/master/ pokinganalyzer_). The software expects an image sequence in which the upper part of each image represents the fluorescence from a calcium indicator inside a cell and the lower part of each image depicts calcium-independent fluorescence inside the same cell (Movie S1†). The cell is selected manually in the first image of each recording in the upper half of the image. The software automatically identifies the cell in the lower half. The following steps are performed in both halves of the image individually. The intensities of the selected cell and its surroundings are analyzed to define thresholds. Using these thresholds, the cell is automatically tracked in the entire image sequence. For background correction, the intensities of the areas surrounding the cell (F_{bg}) are subtracted from the intensities of the cell (F) for each image. The differences are divided by the mean pre-stimulus intensities of the cell (F_0). The results are the background-subtracted normalized fluorescence intensities of the cell ($(F - F_0)/(F_{bg} - F_0)$) in the calcium-dependent and calcium-independent halves of the image sequence. To correct defocusing artifacts, the calcium-dependent fluorescence of the cell ($F_{Ca^{2+}}(t)$) is corrected by:

$$F_{Ca^{2+}}(t) = F_{Ca^{2+}}(t) + \left(\frac{sd_{Ca^{2+}}}{sd_{corr}} \cdot \left(1 - F_{corr}(t)\right) \right), \quad (2)$$

where $sd_{Ca^{2+}}$ is the pre-stimulus standard deviation of the cell's fluorescence in the calcium-dependent channel, sd_{corr} is the pre-stimulus standard deviation of the cell's fluorescence in the calcium-independent channel, and $F_{corr}(t)$ is the cell's fluorescence in the calcium-independent channel.

Author contributions

Acknowledgements

References

1 S. Hughes, S. McBain, J. Dobson and A. J. El Haj, *J. R. Soc., Interface*, 2008, **5**, 855–863.

2 F. Sachs, *Physiology*, 2010, **25**, 50–56.

3 T.-W. Chen, T. J. Wardill, Y. Sun, S. R. Pulver, S. L. Renninger, A. Baohan, E. R. Schreiter, R. A. Kerr, M. B. Orger, V. Jayaraman, L. L. Looger, K. Svoboda and D. S. Kim, *Nature*, 2013, **499**, 295–300.

4 E. A. Reits and J. J. Neefjes, *Nat. Cell Biol.*, 2001, **3**, E145–E147.

5 M. Krieg, A. R. Dunn and M. B. Goodman, *Nat. Cell Biol.*, 2014, **16**, 224–233.

6 A. Freikamp, A. Mehlich, C. Klingner and C. Grashoff, *J. Struct. Biol.*, 2017, **197**(1), 37–42.

7 F. Meng and F. Sachs, *J. Cell Sci.*, 2012, **125**, 743–750.

8 B. D. Hoffman and A. S. Yap, *Trends Cell Biol.*, 2015, **25**, 803–814.

9 M. Chalfie, *Nat. Rev. Mol. Cell Biol.*, 2009, **10**, 44–52.

10 S. Katta, M. Krieg and M. B. Goodman, *Annu. Rev. Cell Dev. Biol.*, 2015, **31**, 347–371.

11 H. Suzuki, R. Kerr, L. Bianchi, C. Frøkjaer-Jensen, D. Slone, J. Xue, B. Gerstbrein, M. Driscoll and W. R. Schafer, *Neuron*, 2003, **39**, 1005–1017.

12 R. O'Hagan, M. Chalfie and M. B. Goodman, *Nat. Neurosci.*, 2005, **8**, 43–50.

13 A. L. Eastwood, A. Sanzeni, B. C. Petzold, S.-J. Park, B. L. Pruitt and M. B. Goodman, *Proc. Natl. Acad. Sci. U. S. A.*, 2015, **15**, E6955–E6963.

14 M. Krieg, A. R. Dunn and M. B. Goodman, *BioEssays*, 2015, **37**, 335–344.

15 M. Kelley, J. Yochem, M. Krieg, A. Calixto, M. G. Heiman, A. Kuzmanov, V. Meli, M. Chalfie, M. B. Goodman, S. Shaham, A. Frand and D. S. Fay, *eLife*, 2015, **4**, 1–30.

16 A. D. Chisholm and S. Xu, *Wiley Interdiscip. Rev.: Dev. Biol.*, 2012, **1**, 879–902.

17 M. Goodman, *WormBook*, 2006, pp. 1–14.

18 M. Chalfie and M. Au, *Science*, 1989, **243**, 1027–1033.

19 C. Frøkjær-Jensen, K. S. Kindt, R. A. Kerr, H. Suzuki, K. Melnik-Martinez, B. Gerstbreih, M. Driscol and W. R. Schafer, *J. Neurobiol.*, 2006, **66**, 1125–1139.

20 M. Chatzigeorgiou, S. Yoo, J. D. Watson, W.-H. Lee, W. C. Spencer, K. S. Kindt, S. W. Hwang, D. M. Miller III, M. Treinin, M. Driscoll and W. R. Schafer, *Nat. Neurosci.*, 2010, **13**, 861–868.

21 R. A. Kerr and W. R. Schafer, in *C. elegans*, Humana Press, New Jersey, 2006, vol. 351, pp. 253–264.

22 M. Shaw, M. Elmi, V. Pawar and M. A. Srinivasan, *Biomed. Opt. Express*, 2016, **7**, 2877.

23 S. E. Hulme, S. S. Shevkoplyas, A. P. McGuigan, J. Apfeld, W. Fontana and G. M. Whitesides, *Lab Chip*, 2010, **10**, 589.

24 R. B. Kopito and E. Levine, *Lab Chip*, 2014, **14**, 764–770.

25 N. Chronis, M. Zimmer and C. I. Bargmann, *Nat. Methods*, 2007, **4**, 727–731.

26 T. V. Chokshi, A. Ben-Yakar and N. Chronis, *Lab Chip*, 2009, **9**, 151.

27 J. Krajniak and H. Lu, *Lab Chip*, 2010, **10**, 1862.

28 E. Kim, L. Sun, C. V. Gabel and C. Fang-Yen, *PLoS One*, 2013, **8**, e53419.

29 S. E. Hulme, S. S. Shevkoplyas, J. Apfeld, W. Fontana and G. M. Whitesides, *Lab Chip*, 2007, **7**, 1515.

30 J. Yuan, J. Zhou, D. M. Raizen and H. H. Bau, *Lab Chip*, 2015, **15**, 2790–2798.

31 S. Johari, V. Nock, M. M. Alkaisi and W. Wang, *Lab Chip*, 2013, **13**, 1699–1707.

32 T. V. Chokshi, D. Bazopoulou and N. Chronis, *Lab Chip*, 2010, **10**, 2758–2763.

33 P. Rezai, A. Siddiqui, P. R. Selvaganapathy and B. P. Gupta, *Lab Chip*, 2010, **10**, 220–226.

34 T. V. Chokshi, D. Bazopoulou and N. Chronis, *Appl. Phys. Lett.*, 2011, **99**, 3–5.

35 M. Cornaglia, G. Krishnamani, L. Mouchiroud, V. Sorrentino, T. Lehnert, J. Auwerx and M. A. M. Gijs, *Mol. Neurodegener.*, 2016, **11**, 17.

36 K. E. McCormick, B. E. Gaertner, M. Sottile, P. C. Phillips and S. R. Lockery, *PLoS One*, 2011, **6**(10), e25710.

37 G. Zhu, F. Yin, L. Wang, W. Wei, L. Jiang and J. Qin, *Integr. Biol.*, 2016, **8**, 30–38.

38 Y. Xia and G. M. Whitesides, *Annu. Rev. Mater. Sci.*, 1998, **28**, 153–184.

39 B. C. Petzold, S.-J. Park, E. A. Mazzochette, M. B. Goodman and B. L. Pruitt, *Integr. Biol.*, 2013, **5**, 853.

40 W. C. Young and R. G. Budynas, *Roark's Formulas for Stress and Strain*, 2002, vol. 7, p. 832.

41 S. J. Lee, J. C.-Y. Chan, K. J. Maung, E. Rezler and N. Sundararajan, *J. Micromech. Microeng.*, 2007, **17**, 843–851.

42 I. D. Johnston, D. K. McCluskey, C. K. L. Tan and M. C. Tracey, *J. Micromech. Microeng.*, 2014, **24**, 035017.

43 C. M. Harris and A. G. Piersol, in *Harris Shock and Vibration Handbook*, McGraw-Hill, New York, NY, 6th edn, 2010, ch. 1.

44 R. D. Schultz and T. L. Gumienny, *J. Visualized Exp.*, 2012, 1–6.

45 W. Gilpin, S. Uppaluri and C. Brangwynne, *Biophys. J.*, 2015, **108**, 1887–1898.

46 A. Ward, J. Liu, Z. Feng and X. Z. S. Xu, *Nat. Neurosci.*, 2008, **11**, 916–922.

47 N. Bhatla and H. R. Horvitz, *Neuron*, 2015, **85**, 804–818.

48 S. L. Edwards, N. K. Charlie, M. C. Milfort, B. S. Brown, C. N. Gravlin, J. E. Knecht and K. G. Miller, *PLoS Biol.*, 2008, **6**, 1715–1729.

49 D. Lockhead, E. M. Schwarz, R. O. Hagan, S. Bellotti, M. M. Barr, A. R. Dunn, P. W. Sternberg and M. B. Goodman, *Mol. Biol. Cell*, 2016, **27**(23), 3717–3728.

50 M. Chalfie, A. C. Hart, C. H. Rankin and M. B. Goodman, *WormBook*, 2014, pp. 1–13.

51 M. Chalfie and J. Sulston, *Dev. Biol.*, 1981, **82**, 358–370.

52 S. Wicks and C. Rankin, *J. Comp. Physiol., A*, 1996, **179**, 675–685.

53 A. M. Leifer, C. Fang-Yen, M. Gershow, M. J. Alkema and A. D. T. Samuel, *Nat. Methods*, 2011, 1–8.

54 T. Stiernagle, *WormBook*, 2006, pp. 1–11.

55 Y. Temiz, R. D. Lovchik, G. V. Kaigala and E. Delamarche, *Microelectron. Eng.*, 2015, **132**, 156–175.